Arch. Metall. Mater. **67** (2022), 1, 57-65

DOI: https://doi.org/10.24425/amm.2022.137472

JIAN ZHOU[1*], HONGKUN XU[1], CHENYU ZHU[1], BIN WANG[1], KUN LIU[1*]

COMPARISONS BETWEEN 2D AND 3D MPFEM SIMULATIONS IN MODELING UNIAXIAL HIGH VELOCITY COMPACTION BEHAVIORS OF Ti-6Al-4V POWDER

Multi-particle finite element method (MPFEM) simulation has been proven an efficient approach to study the densification behaviors during powder compaction. However, comprehensive comparisons between 2D and 3D MPFEM models should be made, in order to clarify which dimensional model produces more accurate prediction on the densification behaviors. In this paper, uniaxial high velocity compaction experiments using Ti-6Al-4V powder were performed under different impact energy per unit mass notated as E_m. Both 2D and 3D MPFEM simulations on the powder compaction process were implemented under displacement control mode, in order to distinguish the differences. First, the experimental final green density of the compacts increased from 0.839 to 0.951 when E_m was increased from 73.5 J/g to 171.5 J/g. Then detailed comparisons between two models were made with respect to the typical densification behaviors, such as the density-strain and density-pressure relations. It was revealed that densification of 2D MPFEM model could be relatively easier than 3D model for our case. Finally, validated by the experimental results, 3D MPFEM model generated more realistic predictions than 2D model, in terms of the final green density's dependence on both the true strain and E_m. The reasons were briefly explained by the discrepancies in both the particles' degrees of freedom and the initial packing density.

Keywords: multi-particle finite element method; Ti-6Al-4V; powder compaction; relative green density; impact energy per unit mass

1. Introduction

Ti-6Al-4V alloy prevails as one of the most commonly used titanium alloys due to its excellent performance and relatively affordable price. However, it is still very challenging to manufacture titanium and titanium alloys using convectional approaches [1]. Great efforts have been made to promote powder metallurgy (PM) into the mass production of titanium alloys for a few decades [2]. In order to guarantee the final PM product quality, it is highly crucial to prepare qualified green compact during powder compaction stage. But titanium alloy powder could be rather difficult to be compressed under normal conditions. Recent years, a newly developed powder compaction technique – high velocity compaction (HVC) was therefore proposed [3,4], where the green powder was compacted by one or several instantaneous high-energy impacts [5]. Compared to the conventional compaction, HVC shows advantages in increasing the green density, improving the mechanical properties and enhancing the possibility to produce large-scale parts [4,6]. Successful experimental attempts have been made to apply HVC technique into the compaction of titanium powder [4,7,8] and titanium alloy powder [9-11]. For connecting the compact's green density with the process parameters of HVC, several quantity indicators have been employed, such as peak pressure [3,11], impact velocity [12,13], impact energy [7,10] and impact energy per unit mass [8]. Among these indicators, impact energy per unit mass notated using E_m, has been demonstrated more reasonable and applicable to characterize HVC, since it is a normalized parameter and reflects the essence of energy conversion as well.

Experimental studies on the powder densification behaviors and the compact's quality performance, are commonly time and cost consuming, especially when the compact's shape is complex or irregular. Simulation approaches not only provide an alternative solution to predict the experimental results with more details, but also furthermore throw light on revealing the particles flow behaviors and the densification mechanisms. Typical simulation schemes for powder compaction, include continuum media approach or finite element method (FEM), discrete element method (DEM) and multi-particle finite ele-

[1] HEFEI UNIVERSITY OF TECHNOLOGY, SCHOOL OF MECHANICAL ENGINEERING, HEFEI, 230009, CHINA

* Corresponding authors: jianzhou@hfut.edu.cn; liukun@hfut.edu.cn

ment method (MPFEM). Combining the advantages of both continuous and discrete schemes, MPFEM was developed to catch the particulate-scale flow and solve the large deformation problem simultaneously [14]. Since the particles are modeled as solid continuum deformable bodies in MPFEM, many advanced material models, such as elastic-plastic with full consideration of rate and temperature dependences, viscoelastic, and hyperelastic, which are provided by the FEM commercial packages, can be directly assigned to the particles. With contrast, in DEM, the particles are typically treated as rigid bodies, hence much extra efforts are required to equivalently characterize complex material models. In addition, comprehensive contact interactions between particles can be developed to well characterize the compressive, tensile and adhesive contact behaviors. Therefore, MPFEM has been employed to investigate the densification mechanisms and flow behaviors [15-19], compare the densification behaviors under different particle sizes and/or size ratios [15,18,20], generate the yield surfaces [21,22], explore the effect of friction behavior [23,24] and other purposes for powder compaction. However, the disadvantage of MPFEM (especially 3D MPFEM) is the extremely high computational costs, which by far exceed the computational cost of DEM with the same number of particles. Therefore, a small portion of the powder compact which is defined as the representative volume element (RVE), can be only modeled.

Two-dimensional analysis has been demonstrated very instructive in studying the compact's green density behaviors during powder compaction [15-20,24-26]. Nevertheless, as clearly stated in the compaction study of tungsten powder, a distinct gap was observed in the density-pressure curve between the prediction of 2D MPFEM model and the experimental result [25]. Moreover, the authors pointed out that the discrepancy was caused by the loss of degrees of freedom (DOF) in 2D model. Therefore, in order to reliably simulate the green density's dependence on the process parameters for HVC, it is a prerequisite to make choice on which model (2D or 3D MPFEM) should be adopted. Hitherto, quantitative comparison between 2D and 3D MPFEM models for a specific powder compaction case has not been thoroughly investigated. Additionally, the materials studied in MPFEM models covered aluminum [18], copper [26], Fe/Al composite [16,24], Al/SiC composite [20] and others. Compared to those easily densified metal powders, densification of Ti-6Al-4V powder is much more difficult due to its strong mechanical strength, and has not been widely investigated. Thus, to the authors' best knowledge, modeling on this powder is still scarce. Moreover, the need for modeling the HVC process is urgent, as the process duration is so short (several milliseconds) that there are limited experimental approaches to monitor the microscale and mesoscale densification behaviors. Therefore, modeling on the HVC process of Ti-6Al-4V powder is of great importance.

In this paper, the main goal is to distinguish which model (2D or 3D MPFEM) is more appropriate to predict the compact's green density behaviors. To this end, both 2D and 3D MPFEM models with almost the same particles' diameter distribution were established under displacement control mode. Uniaxial HVC experiments using Ti-6Al-4V powder were performed under different E_m. Then detailed comparisons were made regarding the compaction behaviors and the dependence of the final green density on E_m. At last, experimental results were introduced to determine which model better fitted the reality. Brief discussions were made to address the underlying reasons.

2. High velocity compaction experiments

The purpose of the HVC experiments is to determine the relation between the final green density of the compacted specimen and E_m for Ti-6Al-4V powder, thus providing data reference to compare the reliability of the following MPFEM simulation results. In this study, the uniaxial powder compaction experiments were performed on the lab-built HVC machine. As presented in Fig. 1(a), the machine is mainly composed of the mold assembly, the impact hammer, the electrical controller and other mechanical supporting parts. The core mold assembly consists of the top punch, the bottom punch and the die. In Fig. 1(b), the whole HVC process is made up of three steps, powder filling, compaction and ejection. First, Ti-6Al-4V powder with mass of 4.0 g is poured into the cavity with diameter of 16 mm, and sandwiched between the top and bottom punches. The initial height h_0 of the loose powder is determined as 9.43 mm, by measuring the positions of the top punch before and after pouring the powder. During compaction, a heavy hammer which is released at a specific height, instantaneously impacts the top punch to compress the powder. The impact energy per unit mass E_m is defined as:

$$E_m = E/m = Mgh/m \tag{1}$$

where M = 50 Kg is the mass of the hammer, H is the initial hanging height of the hammer, and m = 4.0 g is the mass of the Ti-6Al-4V powder. A strain gauge attached to the bottom punch indicates that the duration of the effective compaction process is about 2.0-3.0 millisecond, and this value will guide the following simulation setup. After compaction, the bottom punch is removed, and then the compact is manually ejected by softly knocking the top punch. The density of the compact is measured based on the Archimedes' principle which results in the object's density $\rho = \rho_0 W_0/(W_0 - W_1)$, where ρ_0 is the density of water, W_0 and W_1 are the measured weight of the sample in air and in water respectively.

Here, the Ti-6Al-4V powder was produced using the electrode induction gas atomization (EIGA) technique and supplied by the AMC POWDERS Co. Ltd, Beijing, China. The basic properties and particles' diameter distribution information were provided by the company as listed in Table 1. Here the particle diameter distribution accounts for the number percentage of particles in number whose diameter is less than the given value, for example, D10 at 102 μm indicates that the percentage of the particles with diameter less than 102 μm is 10%. According to the quality check data from the powder provider, the diameter values

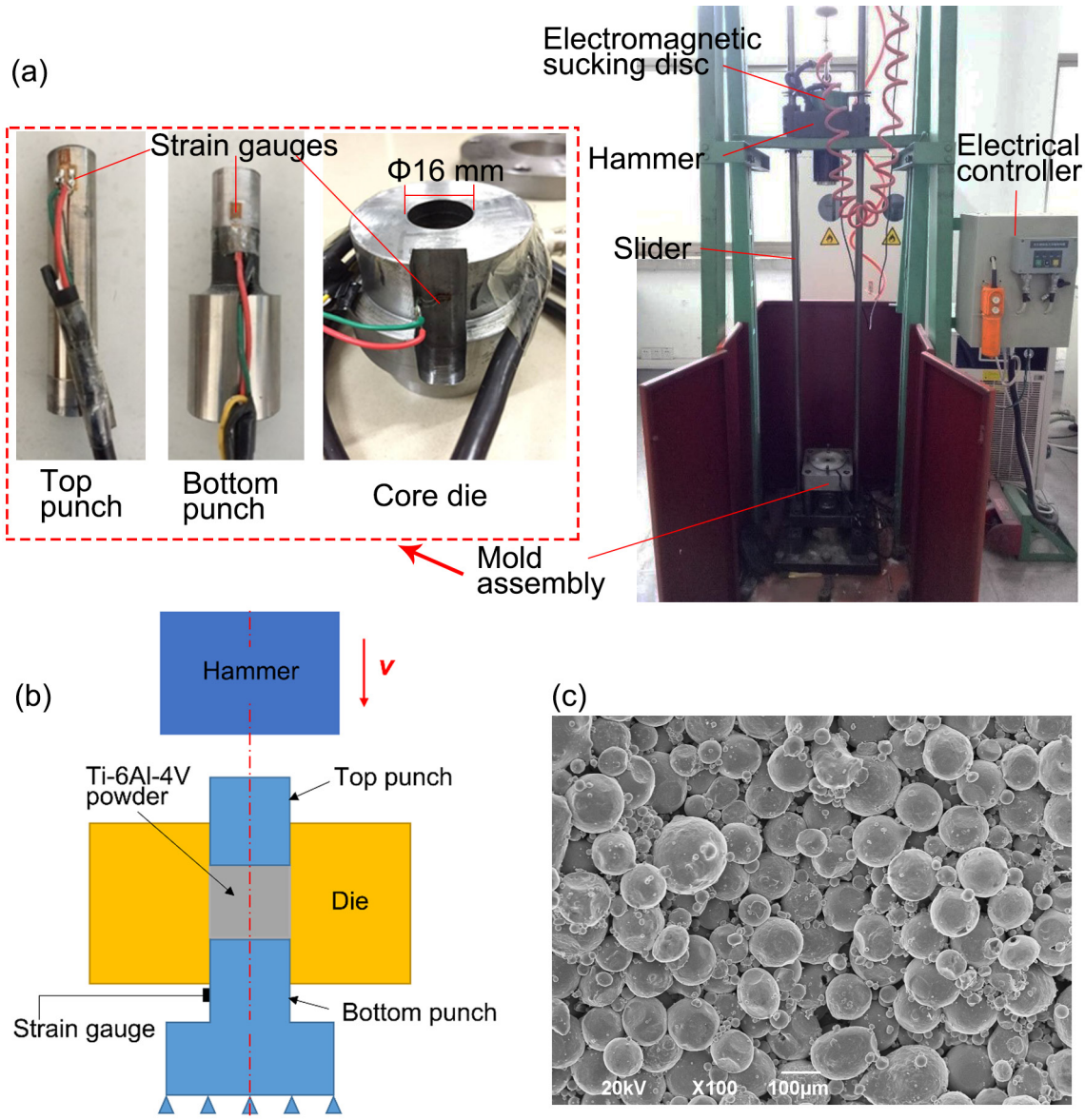

Fig. 1. (a) The components composition of the lab-built HVC machine, (b) the schematic illustration of the uniaxial HVC experiment setup, (c) the SEM micrograph of the Ti-6Al-4V powder (amplification ×100) which was in a considerably dense state

of 80% of the powder particles fall in the range of 102-226 μm. From the SEM micrograph of the powder in a considerably dense state (Fig. 1(c)), though there are a small portion of particles in small size, most particles are big ones with diameter larger than 100 μm.

TABLE 1

Basic properties and particle diameter distribution of Ti-6Al-4V powder

Apparent density (g/cm^3)	Theoretical density (g/cm^3)	Sphere degree	Particle diameter distribution (μm)		
			D10	D50	D90
2.11	4.42	>=0.90	102	152	226
Chemical compositions (wt. %)	Ti	Al	V	C	Others
	88.5%	5.85%	4.10%	0.03%	Balance

3. Implementation of 2D and 3D MPFEM simulations

In this part, details about both 2D and 3D MPFEM models simulating the HVC process were provided. These simulations adopted the displacement control mode, in order to easily achieve the same relative density in the end and hence fulfil the comparison purpose. Due to the limit of computation costs, only a small portion of the real packing was modeled. The initial powder packing was generated in the discrete element method (DEM) software and then imported into Abaqus to implement the MPFEM simulation. The details are described as follows.

Powder packing generation in DEM software: In order to best match the diameter distribution of the simulated particles with reality, commercial DEM codes – *PFC 2D* and *PFC 3D* (*Itasca Inc., Minneapolis, USA*), were employed to generate the initial powder packing. A proper setup for the range of diameter

realized the basic control on particles generation. Moreover, a low cut-off value was set to avoid too small particles. Since the real diameter distribution was close to Gaussian function, the key word *gauss* was included in the particles generation command. Gravity deposition method was adopted to reach equilibrium. Herein, 174 circular discs were generated within the rectangular box with dimensions of 2000×2440 μm for 2D model (Fig. 2(a)). Meanwhile, 135 spheres were generated within the cubic box with dimensions of 800×800×900 μm for 3D model (Fig. 2(b)). Both cumulative histograms of the generated particles' diameter distribution (Fig. 2(c)) were very close to the provided data in Table 1.

MPFEM implementation in Abaqus: After the particles generation in *PFC* codes, the center coordinates and diameters of the generated particles were extracted, and then transferred to regenerate the initial packing in Abaqus via Python scripts. The discs and spheres were deformable, while the walls and punches were defined as rigid bodies. The walls and bottom punch were fixed at all the degrees of freedom. For the displacement control, a time-dependent displacement was applied to the top punch in the vertical direction. The displacements were 525 μm and 440 μm for 2D and 3D models respectively. The compaction duration was chosen as 2.0 ms which was coherent with the experiments. Since the deformation in *z* direction was assumed zero for 2D model, the compaction simulation was defined as plane strain analysis in *xy* plane. Proper meshes were generated for all the deformable particles, herein, 414 quadrilateral plane strain elements were meshed for each disc, and 3936 hexahedral 3D stress elements were meshed for each sphere. The mesh fineness parameter which is defined as the ratio of particle diameter to element size, is usually employed to determine the proper mesh size. According to the mesh fineness investigation in a very similar 3D MPFEM study for powder compaction [22], it was concluded that the simulation results reached good convergence, when the mesh fineness was higher than 8. From the demo meshes for both models in our study (Fig. 2(a) and 2(b)), much greater mesh fineness values were adopted, which were 22 and 15 for 2D and 3D models respectively, thus convergence would be expected with good reason. Because high velocity compaction is an instantaneous impact process, the dynamic explicit

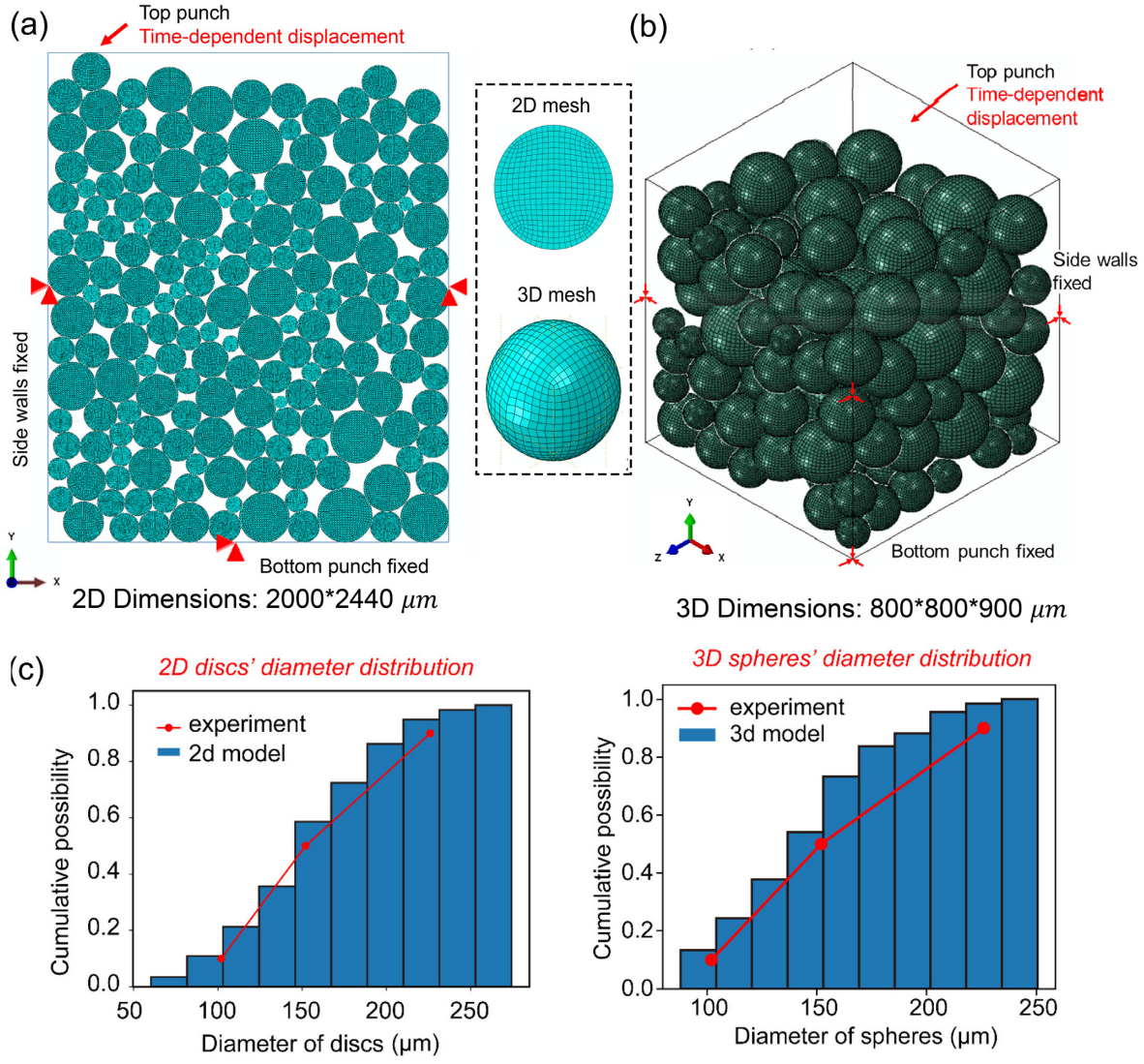

Fig. 2. (a) 2D MPFEM model, and (b) 3D MPFEM model implemented in Abaqus, (c) the histograms of particles' diameter distribution for 2D and 3D models respectively

procedure was adopted. To accelerate the computation speed, a proper mass scaling scheme was also employed.

The Coulomb friction model with penalty formulation and hard contact pressure-overclosure algorithm, were used for both models to characterize the tangential and normal interaction behaviors respectively. Both the wall-particle friction and the interparticle friction could affect the densification behaviors. Since the rigid walls in the models only served as the boundary conditions of the representive volume element (RVE), the wall-particle friction was set zero herein, which is a typical treatment in other references [22,27,28]. On the other hand, it is commonly recognized hard to accurately determine the interparticle friction because of the microscale size, granular rheology and complex dependences on load conditions. Concerning this limitation, four assumed interparticle friction coefficients (0.01, 0.10, 0.20, 0.30) were used in the simulations, in order to reasonably study the effects of interparticle friction. Surface-to-surface contact detection method was applied for 2D model, and possible contact pairs were defined in advance. The automatic general contact detection method was adopted for 3D model.

***J-C* model for Ti-6Al-4V**: The flow stress of metals and alloys strongly depends on strain, strain rate and temperature. Since the HVC process for Ti-6Al-4V was finished within several milliseconds, the strain rate could be so high that the effect of strain rate on the working hardening was significant. This could be one of the basic differences between HVC and conventional compaction. Though the transient temperature of powder could be increased during HVC, the induced temperature effect was neglected here, because the increased temperature is believed to be small enough compared to the melting point of Ti-6Al-4V (1620°C). Therefore, a concise flow stress form of the Johnson-Cook equation removing the temperature dependence was adopted:

$$\sigma = \left(A + B\varepsilon_p^n\right)\left(1 + C\ln\left(\frac{\dot{\varepsilon}}{\dot{\varepsilon}_0}\right)\right) \qquad (2)$$

where A, B, C, n, are constants, ε_p^n is the effective plastic strain, $\dot{\varepsilon}$ is the dynamic strain rate. These parameters for Ti-6Al-4V alloy at room temperature were reported in Ref [29] as listed in Table 2.

TABLE 2

Material properties of Ti-6Al-4V alloy

Elastic modulus (GPa)	Poisson's ratio	Johnson Cook model parameters [29]				
		A (MPa)	B (MPa)	C	n	$\dot{\varepsilon}_0$
112	0.34	870	632	0.032	0.45	10^{-3}

4. Results and discussion

4.1. HVC experimental results

Experiments were conducted under 8 different impact heights from 0.5 m to 1.4 m, and each set of tests were repeated three times. The corresponding E_m was in the range of 61.25-171.50 J/g. The green density values of the complete compacts are presented in Table 3. At E_m = 61.25 J/g, the compact cracked and broke into several pieces, so the density at this point was not accounted.

TABLE 3

Experimental green density values of compacts under different impact heights

No.	Impact height (m)	E_m (J/g)	Compact's height h (mm)	Density (g/cm^3)	Relative density	$-\ln(h/h_0)$
1	0.5	61.25	—	—	—	—
2	0.6	73.50	5.365	3.708	0.839	0.563
3	0.7	85.75	5.350	3.718	0.841	0.566
4	0.8	98.00	5.224	3.807	0.861	0.590
5	0.9	110.25	5.156	3.858	0.873	0.603
6	1.0	122.50	5.057	3.934	0.890	0.623
7	1.2	147.00	4.843	4.107	0.929	0.666
8	1.4	171.50	4.734	4.202	0.951	0.689

The relative green density values of the Ti-6Al-4V powder compacts are plotted against E_m in Fig. 3(a), accompanied with other reported data of titanium and Ti-6Al-4V powder compaction for comparison purpose. The relative green density significantly increased from from 0.839 to 0.951 when E_m was increased from 73.50 J/g to 171.50 J/g. Compared to pure titanium powder, it is observed that a higher E_m is required for Ti-6Al-4V alloy powder to achieve the same relative density, mainly because Ti-6Al-4V alloy is superior to pure titanium in mechanical strength. Taking for example, for titanium powder, 93.5% at 111.7 J/g [4], and 96.0% at 121.7 J/g [8] were reported, while for Ti-6Al-4V in our study, 92.9% at 147 J/g, and 95.1% at 171.5 J/g were determined. On the other hand, our results were close to the reported data in reference [10] where the Ti-6Al-4V powder particles were in irregular shape with a median diameter of 103 μm, but some difference still existed possibly because of the discrepancies in both the size and shape of particles. Therefore, these factors such as powder chemical compositions, particulate size and shape, all could affect the compact density. The images of the compacts are aligned together in Fig. 3(b), and the SEM micrographs of the compact's top surface under four impact heights are presented in Figs. 3(c)-(f). At macroscale, with E_m increasing, the cracks on the compact gradually disappeared, and sound solid compacts were formed when E_m was above 110 J/g. From the microscale viewpoint, the particles were much more extensively deformed at higher E_m, resulting in the significant improvement of density and formability.

4.2. Comparison of densification behaviors between 2D and 3D MPFEM models

The equivalent stress contours at four moments with equal time interval are presented in Fig. 4 where the interparticle friction coefficient is 0.20, in order to show the evolution of

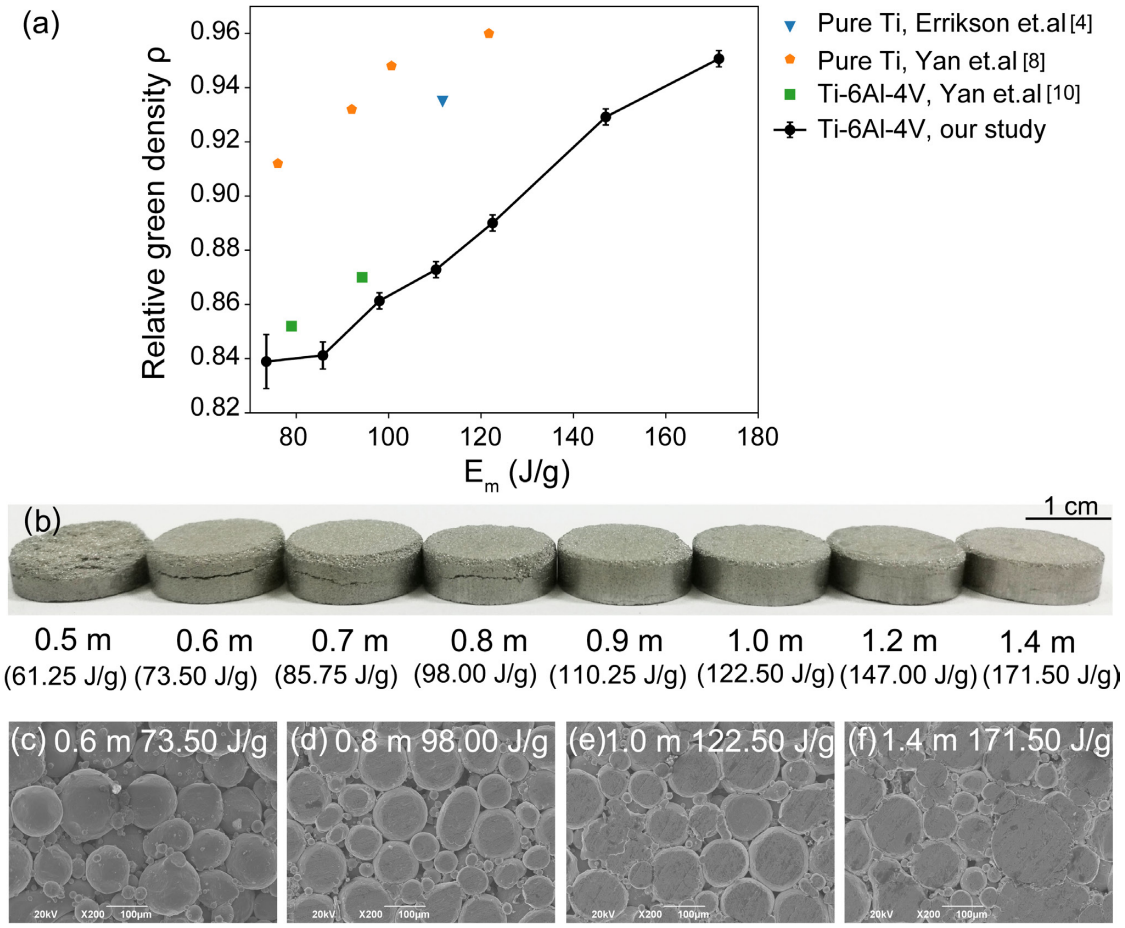

Fig. 3. (a) The relation between the experimental relative density and E_m for Ti-6Al-4V powder, (b) the images of the powder compacts under different E_m, (c)-(f) the SEM micrographs of the compact's top surface under different impact heights

the displacement-controlled compaction process. The relative density of 2D model is calculated using $\rho = A_p/A_{box}$, where A_p is the sum area of all the discs and A_{box} is the area of the rectangular simulation box. For 3D model, the relative density is calculated using $\rho = V_p/V_{box}$, where V_p is the sum volume of all the balls and V_{box} is the volume of the cubic simulation box. The typical pressure-strain and pressure-density relations are plotted in Fig. 5 to characterize the compaction behaviors. To quantitatively compare the compaction behaviors between 2D and 3D models, it is better to use the applied pressure rather than the reaction force. The applied pressure at the bottom surface is calculated using $\sigma_y = F_y/A$, where F_y is the bottom reaction force of the system in the vertical direction, and A is the area of the bottom surface. The true strain of the compact is referred as $\varepsilon = -\ln(h/h_0)$, where h_0 is the initial height of the enclosed box, and h is the changing height during compaction.

Combining Fig. 4 and Fig. 5, for both models, the powder packing system experienced two typical stages, that is, the particles rearrangement and the continuous densification. During the particles arrangement stage, the applied pressure didn't obviously change with the increasing true strain in the starting curve segment of Fig. 5(a). On the contrary, in Fig. 5(b) the relative density began to increase while the applied pressure only slightly increased. Moreover, it seemed that the particles rearrangement was more obvious in 3D model. With further displacement, the powder assembly entered the densification stage. Stress concentration first occurred on the particle-particle and particle-wall contact interfaces. Especially, for the 2D powder packing system, the force chains can be clearly observed at 0.5 ms moment. Then plastic yielding gradually dominated almost all the particles. The applied pressure significantly increased with the true strain. Meanwhile, the porosities were continuously filled so the relative density was increased. Gradually, the slopes of the curves in Fig. 5 became steeper, indicating that further densification turned more difficult. In the end, nearly fully dense compacts were achieved for both models as shown in Fig. 4. Additionally, the effect of interparticle friction was reflected in Fig. 5. For both models, when the interparticle friction coefficient was increased, in order to achieve the same true strain or relative density, a higher external pressure was required, indicating the powder assembly was more difficult to be compressed.

Distinguished from Figs. 5(a) and 5(b), there are discrepancies in the pressure-strain and pressure-density behaviors between 2D and 3D models. Firstly, the true strains required to achieve the nearly fully dense compact were different, approximately 0.24 and 0.65 for 2D and 3D models respectively. Secondly, an obvious gap existed in the initial relative density values, which were about 0.78 and 0.50 for 2D and 3D models

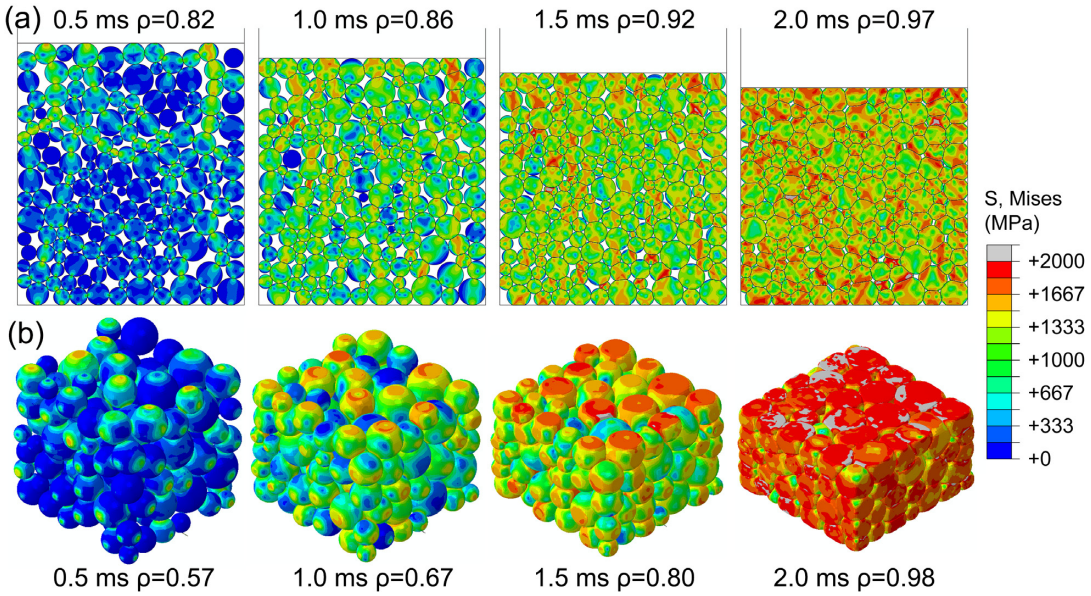

Fig. 4. The equivalent stress contours for (a) 2D model and (b) 3D model at four moments with equal time interval during the displacement-controlled compaction process

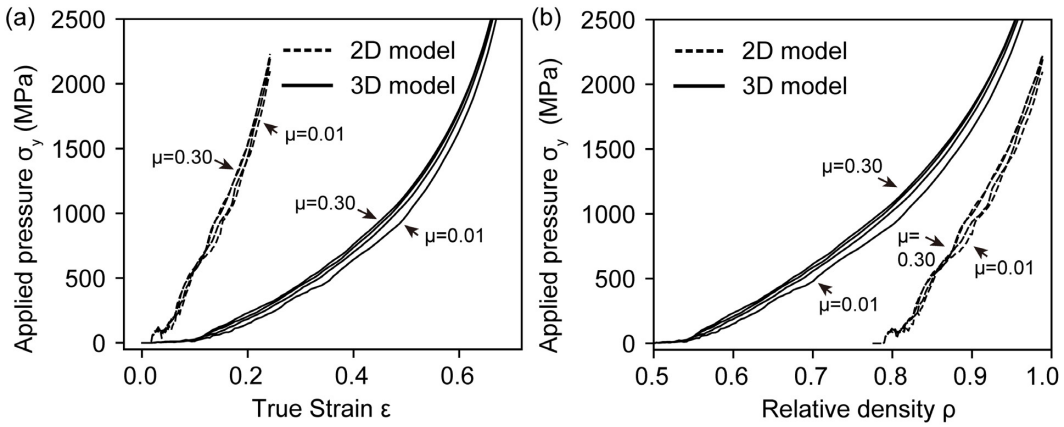

Fig. 5. (a) The relation between the applied pressure and the true strain, (b) the relation between the applied pressure and the relative density for both 2D and 3D models

respectively. As the particle diameter distribution was controlled to be almost the same initially, this gap was probably caused by the intrinsic differences in the spatial dimensions. It is noteworthy that the gap in the initial density between 2D MPFEM and reality has been also observed in other works, for example, the gap is about 0.10 for powder particles with diameter of 5.48 μm [25]; and the gap is 0.25 for random particles assembly with average diameter of 250 μm [27]. From these data, it appears that the discrepancy in the initial density between 2D and 3D models could be related to the diameter distribution. In sum, because of the differences in the required compaction distance and the initial density, the typical pressure-density curves for characterizing the compaction process were separated in Fig. 5(b) between 2D and 3D models. Comparisons made in this part could be helpful to explain the observed discrepancies between 2D MPFEM simulation and experiment.

To further clearly compare the densification difficulty extent between 2D and 3D models, the relation between the relative green density ρ and the applied pressure P was fitted by using the Heckel compaction equation, which is given as below [30]:

$$\ln\left(\frac{1}{1-\rho}\right) = KP + A \tag{3}$$

where A is constant, and K is the slope of the fitting curve. A smaller K indicates it is more difficult to condense the powder packing. In order to reasonably compare the densification performance in the same density range, the fitting data of 3D model started from the initial relative density of 2D model. The fitting results are presented in Fig. 6(a), and the values of the fitting coefficient K are compared in Fig. 6(b). First, the simulation results in Fig. 6(a) were well fitted with good confidence, which validated the reliability of the proposed MPFEM procedures. Since the values of K for 2D model were all greater than 3D model, it was indicated that densification of 2D model was relatively easier than 3D model, which could be caused by the difference in the degrees of freedom under deformation. In addition, for

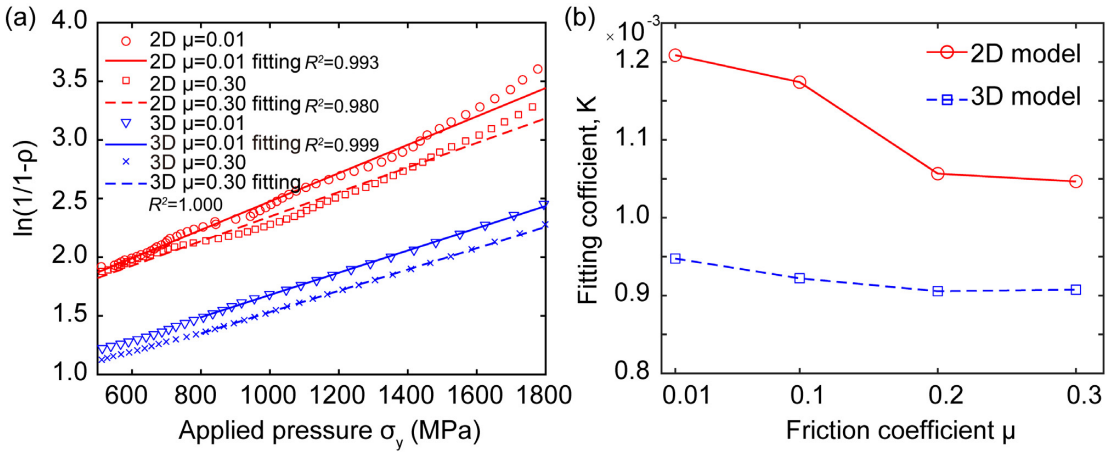

Fig. 6. (a) Fitting curves for the simulation results by using the Heckle equation, (b) the fitting coefficient K at different interparticle friction coefficients for both 2D and 3D models

both models, the fitting slope K decreased with the interparticle friction coefficient, in accord with the common fact that powder densification became difficult when the friction coefficient was increased. Moreover, judging from the decreasing amplitude of K, it was implied that the effect of friction on densification in 2D model could be more significant than 3D model.

4.3. Comparison of the density prediction validated by experiments

Based on the above comprehensive comparisons for two models, in this part, the experimental results were introduced to elucidate which model generated more accurate prediction on the density behaviors. The density-strain relation was compared in Fig. 7(a) from the aspect of the macroscopic deformation extent, meanwhile the dependence of the relative density on E_m was compared in Fig. 7(b). For different interparticle friction coefficients, the density-strain curve was the same because the compaction simulation was controlled by the displacement mode; however, for both models, when the interparticle friction coefficient was increased, more impact energy thus a higher E_m was required to achieve the same density. As observed, the 2D model indicated that an almost fully dense compact was achieved under the true strain of only about 0.24 and at an approximate E_m value of only 56 J/g. However, these predictions generated from 2D model were much less than the experimental results. With contrast, as clearly reflected from both comparisons, the predictions of 3D model were well agreeable with the experimental results within acceptable tolerance. The errors between the 3D model and the experiments could be attributed to several aspects, such as the mismatch of the friction coefficient, the material mechanical properties and the particles' size distribution. Besides, the springback of the compact was not included under the displacement control mode.

Therefore, validated by the experimental results, it was suggested that the 3D MPFEM model generated more realistic predictions than 2D model, in terms of the final density's dependence on both the true strain and E_m. The discrepancies between 2D and 3D MPFEM models, could be explained by the two following aspects: the degrees of freedom (DOF) loss in 2D model and the initial packing density. The balls in 3D model have six

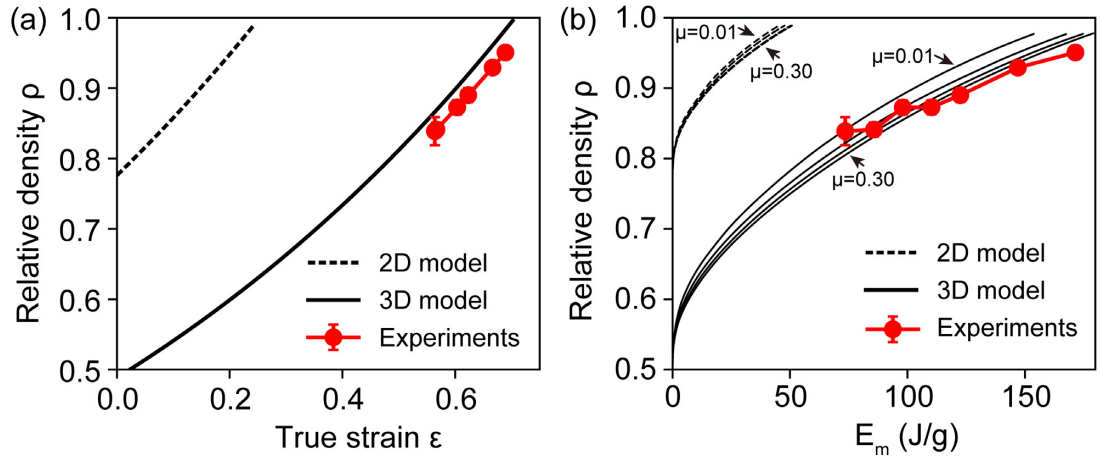

Fig. 7. Comparisons between 2D and 3D models with experimental validation from two aspects: (a) the relation between the relative density and the true strain, (b) the relation between the relative density and E_m

DOF, while the discs in 2D model have only three DOF since the movement in *z* direction was fixed in 2D model. The tight boundary conditions on the discs resulted in a more constrained system, and hence filling the porosities during compaction was relatively easier in 2D model. On the other hand, the relative density of the initial packing was about 0.78 for 2D model, but only 0.50 for 3D model. Since the initial packing density of 2D model was much higher, less displacement and impact energy would be required to accomplish the densification process, which well explained the discrepancies from another aspect.

5. Conclusions

High velocity compaction experiments using Ti-6Al-4V powder were performed under different E_m. The final relative green density of the compacts increased from 0.839 to 0.951 when E_m was increased from 73.5 J/g to 171.5 J/g. Comprehensive comparisons between 2D and 3D MPFEM models were made with regards to the typical densification behaviors, such as the density-strain and pressure-density relations. From the fitting results using the Heckel compaction equation, it was indicated that densification of 2D model could be relatively easier than 3D model for our scenario. Eventually, confirmed by the experimental results, the 3D MPFEM model generated more realistic predictions than 2D model, in terms of the final green density's dependence on both the true strain and E_m. The reasons were explained by the discrepancies in both the particles' degrees of freedom and the initial packing density. Our research would be helpful for providing advice in choosing the proper dimension of MPFEM model to more closely match the simulation results with experiments.

Acknowledgements

The authors are grateful for the financial support from National Natural Science Foundation of China (grant numbers 51905141 and 51975174), Natural Science Foundation of Anhui province (grant number 1808085ME118), and the Fundamental Research Funds for the Central Universities, China (grant number JZ2021HGTB0086). The authors thank Ms. Xia Shu for providing help on using the experiment facilities.

REFERENCES

[1] C. Cui, B. Hu, L. Zhao , S. Liu, Mater. Des. **32** (3), 1684-1691 (2011).

[2] Z.Z. Fang, J.D. Paramore, P. Sun, K.S.R. Chandran, Y. Zhang, Y. Xia, F. Cao, M. Koopman, M. Free, Int. Mater. Rev. **63** (7), 407-459 (2018).

[3] G. Sethi, E. Hauck, R.M. German, Mater. Sci. Technol. **22** (8), 955-959 (2006).

[4] M. Eriksson, M. Andersson, E. Adolfsson, E. Carlstrom, Powder Metall. **49** (1), 70-77 (2006).

[5] J. Johnson, R. German, Int. J. Powder Metall. **4** (1), 201-209 (1993).

[6] D. Yim, W. Kim, S. Praveen, M.J. Jang, J.W. Bae, J. Moon, E. Kim, S.J. Hong, H.S. Kim, Mater. Sci. Eng. A **708**, 291-300 (2017).

[7] M. Eriksson, H,A. Haggblad, C. Berggren, M. Andersson, R. Holmersson, E. Carlstrom, Powder Metall. **47** (4), 335-342 (2004).

[8] Z.Q. Yan, F. Chen, Y.X. Cai, Powder Technol. **208** (3), 596-599 (2011).

[9] D.F. Khan, H.Q. Yin, H. Li, X.H. Qu, M. Khan, S. Ali, M.Z. Iqbal, Mater. Des. **50**, 479-483 (2013).

[10] Z.Q. Yan, F. Chen, Y.X. Cai, J. Yin, Trans. Nonferrous Met. Soc. China **23** (2), 361-365 (2013).

[11] D.F. Khan, H.Q. Yin, H. Li, Z. Abideen, Asadullah, X.H. Qu, M. Ellahi, Mater. Des. **54**, 149-153 (2014).

[12] H. Li, H.Q. Yin, D.F. Khan, H.Q. Cao, Z. Abideen, X.H. Qu, Mater. Des. **57**, 546-550 (2014).

[13] H. Zhang, L. Zhang, G. Dong, Z. Liu, M. Qin, X. Qu, Powder Metall. **59** (2), 100-106 (2016).

[14] R. Ransing, D. Gethin, A. Khoei, P. Mosbah, R. Lewis, Mater Design **21** (4), 263-269 (2000).

[15] P. Han, X.Z. An, D.F. Wang, H.T. Fu, X.H. Yang, H. Zhang, Z.S. Zou, J. Alloys Compd. **741**, 473-481 (2018).

[16] P. Han, X.Z. An, Y.X. Zhang, F. Huang, T.X. Yang, H.T. Fu, X.H. Yang, Z.S. Zou, Powder Technol. **314**, 69-77 (2017).

[17] J. Zhang, Compos. Sci. Technol. **69** (13), 2048-2053 (2009).

[18] K.H. Lee, J.M. Lee, B. M. Kim, Trans. Nonferrous Met. Soc. China **19**, S68-S75 (2009).

[19] A.T. Procopio, A. Zavaliangos, J. Mech. Phys. Solids **53** (7), 1523-1551 (2005).

[20] F. Huang, X.Z. An, Y.X. Zhang, A.B. Yu, Powder Technol. **314**, 39-48 (2017).

[21] B. Harthong, D. Imbault, P. Doremus, J. Mech. Phys. Solids **60** (4), 784-801 (2012).

[22] P. Loidolt, M.H. Uiz, J. Khinast, Powder Technol. **336**, 426-440 (2018).

[23] F. Guner, O.N. Cora, H. Sofuoglu, Powder Technol. **271**, 238-247 (2015).

[24] X. Xin, P. Jayaraman, G. Jiang, R. Wagoner, G. Daehn, Metall. Mater. Trans. A **33** (8), 2649-2658 (2002).

[25] Q. Jia, X.Z. An, H.Y. Zhao, H.T. Fu, H. Zhang, X.H. Yang, J. Alloys Compd. **750**, 341-349 (2018).

[26] Y.X. Zhang, X.Z. An,Y.L. Zhang, Appl. Phys. A **118** (3), 1015-1021 (2015).

[27] Y. Lei, S. Yan, S. Huang, W. Liu, S. Sun, M. Zhou, F. Feng, Journal of Advanced Mechanical Design, Systems, and Manufacturing **12** (1), 17-00619 (2018).

[28] D.R. Kumar, R.K. Kumar, P.K. Philip, Journal of Applied Physics **85** (2), 767-775 (1999).

[29] N.B. Bhalerao, S.S. Joshi, N.K. Naik, J. Eng. Mater. Technol. **140/021009** (2), 1-10 (2018).

[30] R. Heckel, Trans. Metall. Soc. AIME **221** (4), 671-675 (1961).